Cells & Development 171 (2022) 203803

Contents lists available at ScienceDirect

Cells & Development

journal homepage: www.journals.elsevier.com/cells-and-development

A physical model for dynamic assembly of human salivary stem/progenitor microstructures

Yuyang Chen [a], Danielle Wu [b], Herbert Levine [c,*]

[a] Institute of Systems Biomedicine, School of Basic Medical Sciences, Peking University, Beijing 100191, China
[b] The University of Texas Health Science Center at Houston, Houston, TX 77054, USA
[c] Center for Theoretical Biological Physics and Depts. of Physics and Bioengineering, Northeastern University, Boston, MA 02215, USA

ARTICLE INFO

Keywords:
Salivary hS/PC derived microstructure
Tissue expansion
Interface stability

ABSTRACT

The *in vitro* reconstructions of human salivary glands in service of their eventual medical use represent a challenge for tissue engineering. Here, we present a theoretical approach to the dynamical formation of acinar structures from human salivary cells, focusing on observed stick-slip radial expansion as well as possible growth instabilities. Our findings demonstrate the critical importance of basement membrane remodeling in controlling the growth process.

1. Introduction

There has been much interest of late in both the biology and biophysics communities in the problem of epithelial tissue growth. Growth and possible patterning of epithelial tissues are critical both for *in vivo* developmental processes governing organ morphogenesis as well as *in vitro* tissue engineering protocols (Lemke and Nelson, 2021; Torras et al., 2018). From the scientific perspective, the interplay of tissue scale mechanical effects with cellular aspects of division and active motility is still an area of significant challenge (Gompper et al., 2020; Lenne et al., 2021).

Epithelial tissues *in vivo* come in a variety of types, either single layered or stratified. The tissue is surrounded by a basement membrane (BM) composed of biopolymers such as collagen IV and laminin, all of which lies in a surrounding mesenchyme (Pozzi et al., 2017; Sekiguchi and Yamada, 2018). In many cases, cell division events are localized in a thin layer adherent to the basement membrane (BM), within reach of various secreted growth factors. Buckling morphogenesis can arise from the fast expansion of a surface epithelial sheet constrained by adjacent tissues and matrix (Nelson, 2016). An *in vitro* analog of this process can be studied by embedding epithelial cells inside a relatively rigid hydrogel casing (Trushko et al., 2020). The formation of branches *via* this instability has been the focus of much experimental and theoretical effort (Hannezo et al., 2014).

Unlike the development of natural organs or the reconstituted stratified epithelial tissues constructed using rudimentary gland buds (Wang et al., 2021), stem/progenitor cells-derived microstructures originate from single microclusters and have a relatively large proportion of proliferative cells. This rapid cellular proliferation causes the structure to expand rapidly, to push against its surroundings, and to induce active remodeling of the BM (Wu et al., 2019). Understanding the formation, growth and maintenance of these distinct microstructures is important for precise size and shape control in epithelial tissue engineering (Torras et al., 2018). A theoretical description of the tissue expansion process in this biological system as well as the relationship between unperturbed growth and possible interface instabilities are still lacking.

Here, we propose a hydrodynamic model to analyze the growth of a human salivary stem/progenitor microstructure and the stability of its expanding interface. We focus particularly on the effects of BM mechanical properties and dynamics in those processes. Our model reproduces the non-linear expansion and cyclic popping of the microstructure observed in recent experiments (Wu et al., 2019). It also demonstrates the stabilizing and destabilizing factors of the interface, providing a potential explanation to the stable interface maintained by the tissue-engineered salivary gland. These results can also give insights to the dynamics of epithelial tumors since these have similar structural properties (Taubenberger et al., 2019; Laurent et al., 2013; Fiore et al., 2020).

* Corresponding author.
E-mail address: h.levine@northeastern.edu (H. Levine).

https://doi.org/10.1016/j.cdev.2022.203803
Received 11 April 2022; Received in revised form 19 July 2022; Accepted 29 July 2022
Available online 3 August 2022

2. Hydrodynamic theory

Our modeling effort is motivated by recent studies of the growth of a salivary gland microstructure as a step towards the engineering of replacement organs for patients (Wu et al., 2019). An example of this type of structure is shown in Fig. 1. Experiments show that this epithelial tissue is elastic and solid-like at short time scales due to the contractile cytoskeleton networks and adhesion junctions between cells. At long time scales, however, tissue effectively behaves as a viscous fluid, since the residual stresses can be relaxed by cell rearrangements induced by cell division and cell apoptosis (Ranft et al., 2010; Marchetti et al., 2013; David et al., 2012). We therefore use a hydrodynamic formulation, as now will be discussed in detail.

To proceed, we focus on the cell proliferation-induced expansion and long-time behavior of the expanding set of cells. Note that a salivary microstructure, such as the one shown in the figure above, typically takes several days to grow before reaches its maximum size, well within the time scale where the fluid-like behavior should be dominant (Wu et al., 2019). For simplicity, we will treat the system in two-dimensions, instead of dealing exactly with the flattened hemispherical geometry. We therefore model the reorganized epithelium as a circular cylindrical viscous fluid with radius R, surrounded by an elastic BM shell with Young's modulus E and thickness h. With these assumptions, the cell density ρ and the cell velocity field $\vec{v}$ obey the equation.

$$\frac{\partial \rho}{\partial t} + \nabla \cdot \left(\rho \vec{v} \right) = k_p \rho, \tag{1}$$

where k_p is the net division rates of cells. For simplicity, we assume the cell density is essentially constant and the epithelium is incompressible. In this case, the density conservation equation then becomes

$$\nabla \cdot \vec{v} = k_p. \tag{2}$$

We start by assuming that the structure will be rotationally symmetric, *i.e.* all the physical quantities are only functions of the radial position. The inertia of the tissue is also considered negligible. Therefore, the equations of conservation and force balance in the radial and circumferential directions are (see Materials and methods)

$$\frac{1}{r}\frac{\partial (r v_r)}{\partial r} = k_p, \tag{3}$$

$$-\frac{\partial p}{\partial r} + 2\eta \frac{\partial k_p}{\partial r} = 0, \tag{4}$$

$$\frac{\partial}{\partial r}\left[\frac{1}{r}\frac{\partial (r v_\theta)}{\partial r} \right] = 0, \tag{5}$$

where p is the hydrostatic pressure and η is the viscosity of the cellular fluid.

The boundary conditions are determined as follows. In multicellular spheroid structures, epithelial cells polarize and surround a hollow central lumen of finite size (Wu et al., 2019; Tanner et al., 2012; Wang et al., 2013). We assume the size of the lumen remains constant after its formation and the radial velocity vanishes at the inner surface, therefore obtaining the kinematic boundary condition

$$v_r|_{r=r_0} = 0, \tag{6}$$

where r_0 is the radius of the lumen. At the epithelium-BM interface, the elastic stress due to BM deformation is balanced by the normal stress from the fluid. For simplicity, we only consider the small deformations of BM and neglect the compressive stress from the surrounding hydrogel since BM is orders of magnitude stiffer than most hydrogel systems (Wu et al., 2019; Ghosh et al., 2005; Chaudhuri et al., 2020). The normal stress balance at interface then becomes

$$\sigma_{rr}\Big|_{r=R} = \left(-p + 2\eta \frac{\partial v_r}{\partial r} \right)\Big|_{r=R} = -\frac{E\varepsilon h}{R}, \tag{7}$$

where ε is the strain of BM.

The model so far assumes that the motion is purely radial. In fact, however, spontaneous collective revolution of cells within spherical structures is another distinct feature observed in multiple epithelial morphogenesis systems (Wu et al., 2019; Tanner et al., 2012; Wang et al., 2013; L and David, 2011; Horne-Badovinac, 2014). As expected, integrin-mediated traction force applied to the BM by the basal side of the cells is essential for this effective tissue rotation (Wu et al., 2019; Wang et al., 2013). The shear stress at the epithelium-BM interface is just due to this traction exerted by the cells on the BM, and we take to equal the difference between the friction and the active propulsion (Banerjee and Marchetti, 2019; Notbohm et al., 2016).

$$\sigma_{r\theta}\Big|_{r=R} = \eta\left(\frac{\partial v_\theta}{\partial r} - \frac{v_\theta}{r} \right)\Big|_{r=R} = -\xi v_\theta + f_0, \tag{8}$$

Here ξ is the friction coefficient with the BM that depends on the rate of integrin turnover and f_0 is the propulsion force per unit arc length that in 2D determines the direction and magnitude of rotation. For simplicity, these two parameters are taken as constants in our model. We discuss how they may change with tissue growth and how this change may affect the rotational speed in the SI. Based again on the experimental data, we assume the core of the microstructure is jammed (Han et al., 2019) and therefore the rotation vanishes at a finite distance R_J from the BM

$$v_\theta|_{r=R-R_J} = 0. \tag{9}$$

This then completes our specification of the hydrodynamic model. Note that the jamming assumption is only valid for relatively organized microstructures with radius larger than $r_0 + R_J$ (20 μm in our model) and we neglected the initial stages of epithelial morphogenesis (day 1 and day 2 in Fig. 2(c)) in the main text. Additional analysis and a modified boundary condition for the case $R < r_0 + R_J$ is provided in the Supplementary Discussion.

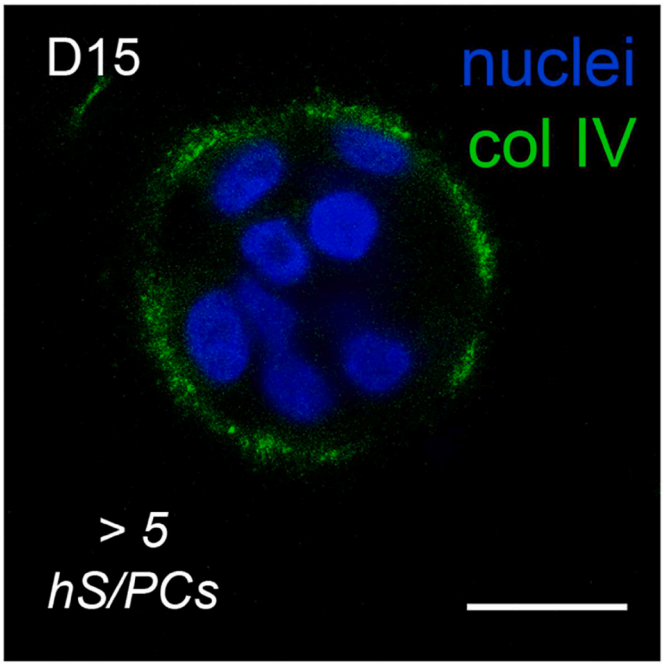

Fig. 1. A typical microstructure formed from human salivary progenitor cells. Blue regions are nuclei and collagen IV is shown in green; this collagen is part of a basement membrane structure formed during the expansion process. The scale bar = 20 μm; taken from (Wu et al., 2019). (For interpretation of the references to color in this figure legend, the reader is referred to the web version of this article.)

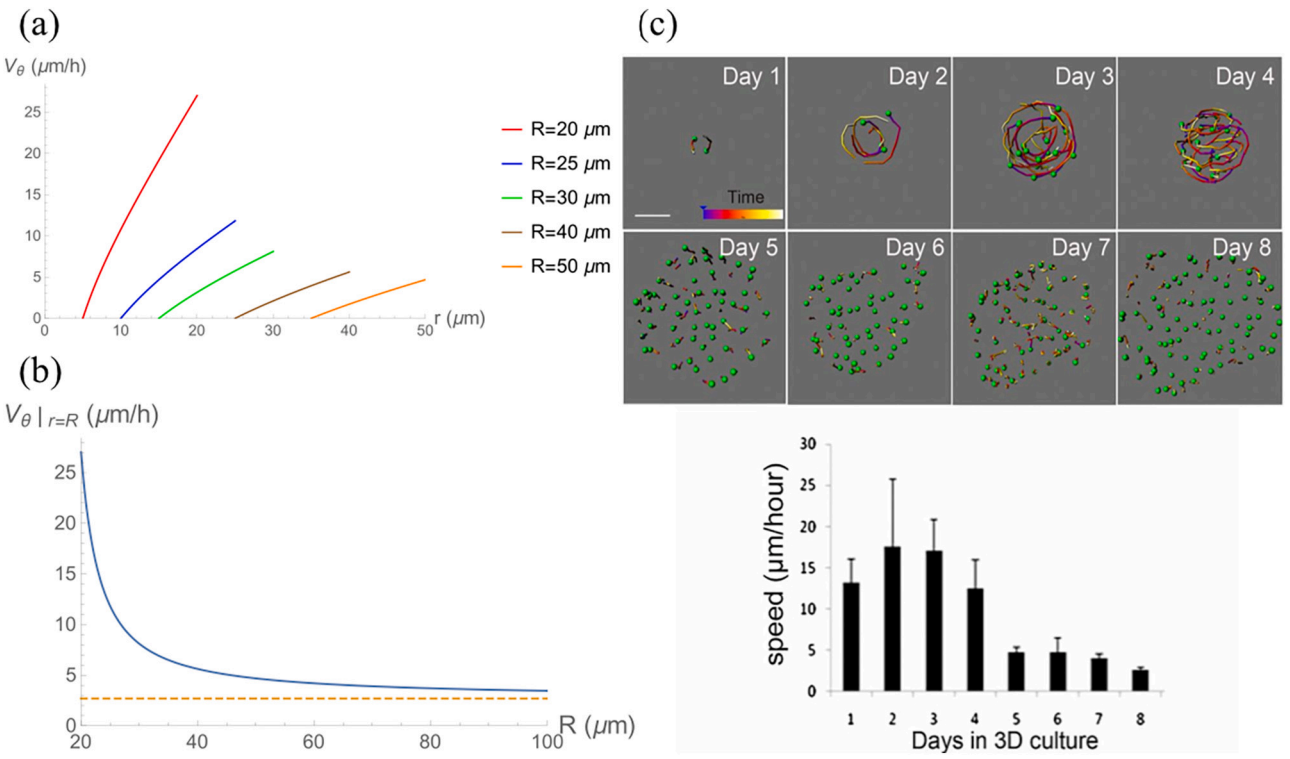

Fig. 2. (a) Tangential velocity profile along radial direction in microstructures with different radiuses. (b) The tangential velocity of surface cell layer in microstructures with different radiuses, which agrees with the rotational speeds measured in (Wu et al., 2019; Wang et al., 2013). (c) Coordinated rotational motion occurs during early stages of MCF-10A 3D morphogenesis. Upper panel: analysis of cell movement in MCF-10A acini. Lower panel: MCF-10A speed analysis. Image in (c) adapted from (Wang et al., 2013).

We first derive the expression of tangential velocity v_θ by solving Eq. (5) with the boundary conditions given in Eqs. (8) and (9). The tangential velocity profile of growing microstructures with different size is shown in Fig. 2(a). v_θ increases nonlinearly along the radial direction and reaches a maximum at the surface cell layer. Furthermore, rotation drastically decreases as the microstructure expands. The exact solution of v_θ at the epithelium-BM interface is

$$v_\theta|_{r=R} = \frac{f_0 R(2R - R_J)R_J}{2R_J^2\eta + 2R^2(\eta + R_J\xi) - RR_J(4\eta + R_J\xi)}. \tag{10}$$

as illustrated in Fig. 2(b). In the limit $R\to\infty, v_\theta|_{r=R}\to\frac{f_0 R_J}{\eta+R_J\xi}$. This result is consistent with the experimental data that coordinated rotational motion are only observed during early stages of microstructure morphogenesis (Wu et al., 2019; Wang et al., 2013) (Fig. 2(c)). In sufficiently large structures, the active propulsion force f_0 exerted by the actomyosin cytoskeleton at a surface cell's leading edge fails to generate enough traction force to overcome the mechanical load of the cells located further inward and hence cannot drive directed collective migration. Hence, the rotations slow down as the structures continue to grow and eventually stops or perhaps decays to random movement.

Next, we discuss the radial velocity and numerically decipher the dynamics of microstructure expansion. The net production rate of cells, k_p, depends on the local concentration of available nutrients and also on the mechanical stress. Nutrients and oxygen diffuse into the epithelium from the BM. The gradients of substances necessary for cell division give rise to gradients of proliferation (Basan et al., 2011; Risler and Basan, 2013). Aside from the supply of nutrients, mechanical stress also has strong impact on multicellular aggregate growth. Numerous experiments have demonstrated that the cell division rate is substantially reduced by external mechanical compression (Taubenberger et al., 2019; Delarue et al., 2013; Dolega et al., 2021; Montel et al., 2012). Hence, we take the net production rate of cells to be given by the following expression:

$$k_p(r) = \frac{k_0}{1 + \left[\alpha\left(-\sigma_{rr}|_{r=R}\right)\right]^m} exp\left(\frac{r-R}{l}\right) = k{\cdot}exp\left(\frac{r-R}{l}\right), \tag{11}$$

where $\sigma_{rr}|_{r=R} = -E\varepsilon h/R$ is the compressive normal stress exerted by BM to the fluid surface. The net cell production is taken to decrease exponentially over a length scale l with increasing distance from the epithelium-BM interface and also depends negatively on the compressive stress with cooperative exponent m.

One additional important relationship between the ability of microstructures to rotate and their ability to assemble BM has to be taken into account. Previous experiments have demonstrated that coordinated rotational motion during microstructure growth is directly associated with secretion and organization of *de novo* BM, especially the assembly of laminin (Wu et al., 2019; Wang et al., 2013; L and David, 2011; Horne-Badovinac, 2014). Microstructures that fail to rotate are defective in production of BM, probably due to insufficient mechanotransduction through cell-matrix adhesions, while artificial dissolution of BM around mature, non-rotating microstructures restores rotational movement and the ability to assemble new BM (Wu et al., 2019; Wang et al., 2013). We therefore need to have a phenomenological approach to BM dynamics. Based on this evidence, we assume that there is BM secretion rate per unit arc length proportional to the tangential velocity at surface when $v_\theta|_{r=R}$ lies above a certain threshold

$$g\left(t\right) = \begin{cases} g_0{\cdot}\left[1 + \beta\left(v_\theta|_{r=R} - v_{\theta\,\text{threshold}}\right)\right] & v_\theta|_{r=R} > v_{\theta\,\text{threshold}} \\ g_0 & v_\theta|_{r=R} \le v_{\theta\,\text{threshold}} \end{cases} \tag{12}$$

where g_0 is the basal net production rate of BM, β controls the strength of rotation-induced secretion rate enhancement and $v_{\theta threshold}$ is the minimum threshold where cells can respond to the mechanical signaling.

As the BM matures, the stiffness of BM positively relates to the total amount of BM per unit arc length

$$E(t) = E_0 \cdot \left(\int_0^t g(t)dt \right)^c, \tag{13}$$

where exponent c represents the influence of the coordination of cross-links between BM components (Chang and Chaudhuri, 2019; Khalilgharibi and Mao, 2021). The new materials are assumed to increase the thickness of BM without changing its density (Khalilgharibi and Mao, 2021), so the thickness of BM h can be expressed by the total volume divided by the surface area

$$h(t) = \frac{2\pi R_0 h_0 + \int_0^t 2\pi R(t) g(t)/\rho dt}{2\pi R(t)}. \tag{14}$$

Substituting Eqs. (11)–(14) into Eq. (3) and imposing the boundary condition Eq. (6), we obtain the solution for the radial velocity v_r. Therefore, the surface growth as a function of time can be obtained by numerically integrating

$$\frac{dR}{dt} = v_r\Big|_{r=R}. \tag{15}$$

The only piece left before this can be carried out is a specification of the tensile strain in the BM.

Since the growth rate prefactor $k = \frac{k_0}{1+[\alpha E \varepsilon h/R]^m}$ is directly related to the time-dependent properties of BM, we begin with two extreme scenarios. If the existing cross-links between different BM components do not remodel when new materials incorporate into the network, the BM will constantly accumulate internal tensile stress as the current length of the tissue boundary increased beyond the constant equilibrium length of the BM. Due to the stress continuity at epithelium-BM interface, k will decrease in response to the compressive stress at surface and the microstructure growth will be drastically inhibited at a small size (Fig. S2(a)-(b)). This scenario is inconsistent with the observed continuous expansion during early stages of microstructure organization (Wu et al., 2019; Wang et al., 2013). One the other hand, if the BM continuously remodels with the tissue expansion and the equilibrium length is always adapted to the size of the microstructure, no tensile stress will accumulate in BM. In that case, the net division rate of the cells will not be suppressed and the radial velocity at tissue boundary will continue to monotonically increase as the microstructure expands (Fig. S2(a)-(b)). This is also in contradiction to the experimental results that all microstructures with tightly organized BM rarely exceed diameters larger than 200 μm, similar to dimensions of acinar structures in normal human tissue (Wu et al., 2019).

To recapitulate the essence of the nonlinear growth curve in experiments, an intrinsic dynamical property of BM has to be incorporated. Specifically, BM has a maximum tensile strain it can bear before breaking (Wu et al., 2019; Chang and Chaudhuri, 2019; Khalilgharibi and Mao, 2021). Upon reaching the threshold, the weak crosslinking points connecting the laminin and collagen IV network can break through exposure to mechanical stress and thereby dissipate stress. Subsequent rebinding of these bonds will result in BM remodeling (Khalilgharibi and Mao, 2021). Therefore, we define a constant ultimate BM tensile strain $\varepsilon_{threshold}$ in our model. The current strain is $\varepsilon = \frac{2\pi R(t) - L_{eq}}{L_{eq}}$, where L_{eq} is the equilibrium length of the BM and $R(t)$ is the current radius of the microstructure. When $\varepsilon < \varepsilon_{threshold}$, BM is pushed by the cells inside and stretched without remodeling. When $\varepsilon = \varepsilon_{threshold}$, BM breaks and remodels simultaneously, reaching a new equilibrium shape configuration. The equilibrium length of BM after remodeling then reads $L_{eq}' = L_{eq}(1 + \varepsilon_{threshold})$.

Substituting the expression for ε into Eq. (11) and solving the above equations for radial expansion, we can numerically obtain the radius of microstructure as a function of time. As demonstrated in Fig. 3(a), the expansion process can be divided into two phases. In phase 1, coordinated rotation exists and BM stiffness increases rapidly due to the rotation-induced BM secretion (Fig. S2(c)). Since the BM still retains its initial assembly and the stiffness is still relatively small, the growth inhibition effect due to compression is insignificant when the tensile strain of BM approaches the threshold (Fig. S2(d)). Thus, the microstructure expands quickly and smoothly during early stages of growth. In phase 2, the tangential velocity reaches the minimum threshold $v_{\theta threshold}$ and the global rotation decays to random motion even as the microstructure continues to grow. The BM secretion rate of cells returns to the basal level. As the BM has now acquired a relatively large stiffness, a significant popping behavior of BM appears. The compressive stress drastically suppresses the net division rate of cells as BM accumulates tensile strain. The expansion slows down to a plateau and spends a long time before reaching the ultimate tensile strain. Upon reaching $\varepsilon_{threshold}$, the weak bonds in BM break and the stretching tension is immediately relaxed. The growth inhibition is thereby relieved and this leads to a rapid expansion pulse, following by a new round of BM organization and tension accumulation. During the short period of rapid expansion, the rate of tissue expansion exceeds the rate of BM production, resulting in a transient BM thinning (Fig. S2(e)). These are consistent with the cyclic thinning and popping of BM detected in the experiments (See Fig. 3(b)). However, there is an apparent difference in time length of the popping events between the experiments and the simulation. This difference in timescales can be rectified by choosing a different basal net cell production rate k_0, as shown in Fig. S3. This parameter choice issue is addressed in Supplementary Discussion. When the stiffness of the BM

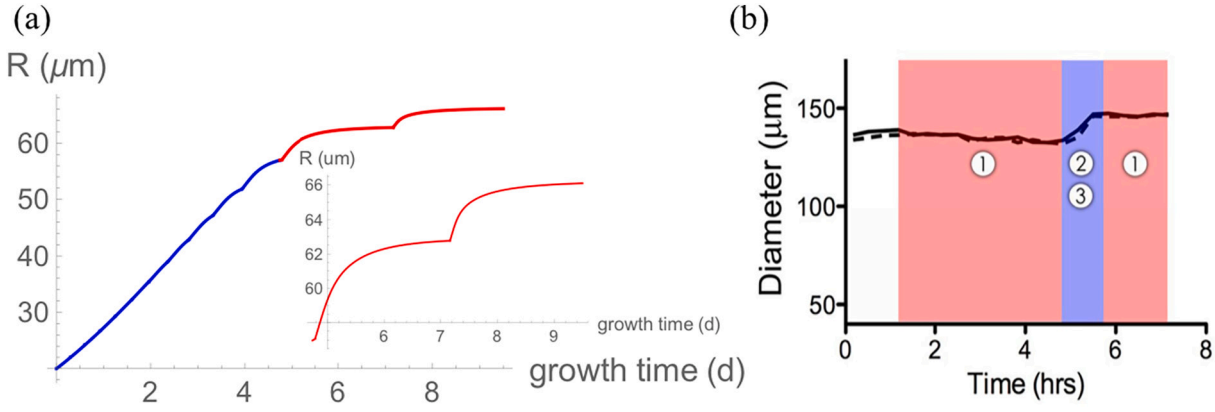

Fig. 3. (a) The increasing radius of the microstructure as a function of time. Blue curve and red curve represent the dynamics of microstructure expansion in phase 1 and phase 2 correspondingly. Inset: detailed view of the microstructure growth curve in phase 2. (b) The popping behavior of human salivary microstructure observed in experiments. Region 1: BM accumulates tensile stress while microstructure expands slowly due to the compression-induced growth inhibition. Region 2 and 3: BM breaks and remodels to relax stress while microstructure expands rapidly. Image adapted from (Wu et al., 2019). Parameters are given in the SI Parameter table. (For interpretation of the references to color in this figure legend, the reader is referred to the web version of this article.)

becomes even larger, the proliferation rate is not enough for the cells to push the BM outward to reach the next breaking point. The microstructure then maintains its current diameter and stops further expansion, providing an accurate mechanical feedback control of tissue size.

3. Microstructure stability calculation

After analyzing the tissue expansion in a radially symmetric state, we now address the question of the interfacial stability of the system. We therefore derive the linearized form of equations governing small perturbations around the previously determined base state. The complicated form of these equations is presented in the SI.

We will carry out the stability calculations with a variety of simplifications. First, we will use quasi-static approximation in which the microstructure radius is assumed to be a constant. This is reasonable once the radius becomes large and the expansion slows (Wu et al., 2019); it is probably not reasonable during the early stages. Now recall that the tangential velocity becomes rather small and effectively stops (Wu et al., 2019; Wang et al., 2013). We therefore have also ignored the role of this velocity component and focus exclusively on a base state with radial motion. In general, we expect that the v_θ terms will tend to stabilize the interface by advecting away any growing shape perturbation, but this needs to be directly established in future work.

One can imagine possible causes of morphological instabilities at the interface of microstructures such as ours, with multilayered proliferating cells. A possible hydrodynamic instability originates from the viscous shear stress arising due to the cell production gradient (Eq. (11)) in expanding cell spheres. This mechanism is similar to the mechanisms underlying undulating or fingering structures in flat stratified epithelium (Basan et al., 2011; Risler and Basan, 2013; Yeh and Chen, 2016), but different from the buckling instability in confined single-layered epithelium induced by the accumulation of in-place compression (Trushko et al., 2020; Hannezo et al., 2012; Hannezo et al., 2011), or the active fingering at the advancing monolayer front driven by collective cell migration (Alert et al., 2019; Williamson and Salbreux, 2018; Yang and Levine, 2020; Pham et al., 2011; Bogdan and Savin, 2018; Mark et al., 2010; Büscher et al., 2020).

In more detail, at the outer boundary we set $r = R + \delta w$, where δw is a small deformation, and neglect the angular velocity in perturbed state for now. Note that the net production rate k_p reaches the same maximum at outer boundary and has no dependence on direction since we consider the nutrient as sufficient and homogeneous outside the BM. The radial velocity in the microstructure then reads

$$\frac{1}{r}\frac{\partial(r\cdot v_r)}{\partial r} = \frac{1}{r}\frac{\partial\left(r\cdot\left(v_r^0 + \delta v_r\right)\right)}{\partial r} = k_p\Big|_{r-\delta w}$$

The distribution of v_r along the radius in perturbed state is showed in Fig. 4(a)-(b). At each radial position, the v_r in the direction where $\delta w<0$ is larger than the v_r in the direction where $\delta w>0$. Therefore, $\frac{\partial v_r}{\partial \theta}$ is nonzero in the presence of an interface perturbation, which gives rise to the radial shear stress within the microstructure. This shear stress enhances the already existing protrusions outwards and promotes the growth of the perturbation. Therefore, the maximal net proliferation rate k and the viscosity of the tissue η have similar destabilizing effects that hinders the relaxation of the interface towards the steady state.

To verify this picture, we carry out a complete analysis of the linear stability problem; details are presented in the SI. The stability spectrum can be seen in Fig. 4(c)-(d) showing the maximum growth rate and the range of unstable wave numbers. As discussed above, the instability is more pronounced at higher viscosity (c) and higher growth rate (d). The increase of these two parameters suggests the tissue has more active cell division and rearrangement, resulting in higher shear stress and supporting a more favorable interfacial configuration that has more access to the nutrients in some directions. Furthermore, the change is more

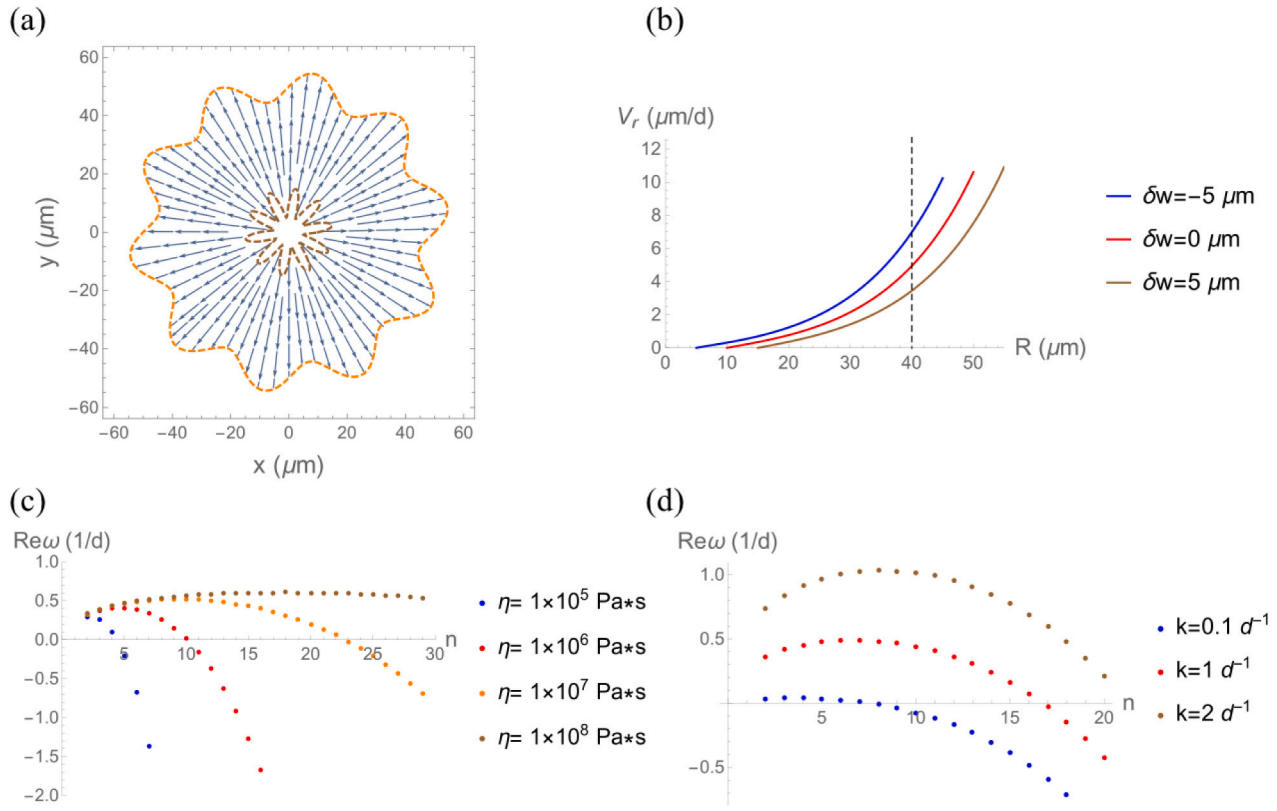

Fig. 4. (a) Schematic representation of the radial velocity field in the presence of an interface perturbation. (b) Radial velocity distributions for different normal deformations at the tissue boundary. The dotted line indicates a specific radial position inside the microstructure. (c) Relaxation modes ω as a function of the azimuthal wavenumber n for different tissue viscosities. (d) Relaxation modes ω as a function of the azimuthal wavenumber n for different net proliferation rates.

prominent at large wave numbers. The most unstable wave number n_{max} decreases as η or k decreases and the interface is more likely to evolve into wider fingers with wavelength $\lambda = \frac{2\pi R}{n}$. This result is consistent with the interpretation that thinner fingers have higher local curvatures and stretch the elastic BM more than wider fingers of the same amplitude. As a result, BM disproportionately resists deformations of thinner fingers with larger strain energy and amplifies the perturbations with longer wavelength (Li and Manikantan, 2021).

Another key observation is that the increasing radius of the microstructure has a destabilizing effect. As shown in Fig. 5(a)-(e), the maximum growth rate of the perturbation increases with increasing size of the microstructure. On the contrary, the increasing Young's modulus of the BM as well as its tensile strain act to retard the instability, due to the decreasing k and to the larger strain energy stored in elastic deformation; these tend to stabilize an interface with higher curvature. This pair of opposite factors provides a potential mechanism that helps to suppress the undesirable interfacial instabilities during microstructure assembly, which is crucial to the precise size and shape control when reestablishing functional tissue *in vitro*.

To understand how this suppression would work, we depict the maximum growth rate of perturbations in Fig. 5(f). The dark blue region representing a smaller ω_{max} localizes in the upper left corner of the stability diagram, where the stiffness of BM is high and the radius of the tissue is small. As shown in Fig. 5(a)-(e), as BM stiffness increases, the fastest-growing wave number n_{max} decreases until finally n_{max}=2, which corresponds to an elliptical boundary. The decrease of ω_{max} is fast when n_{max} is large, but gradually slows down when n_{max} becomes close to 2

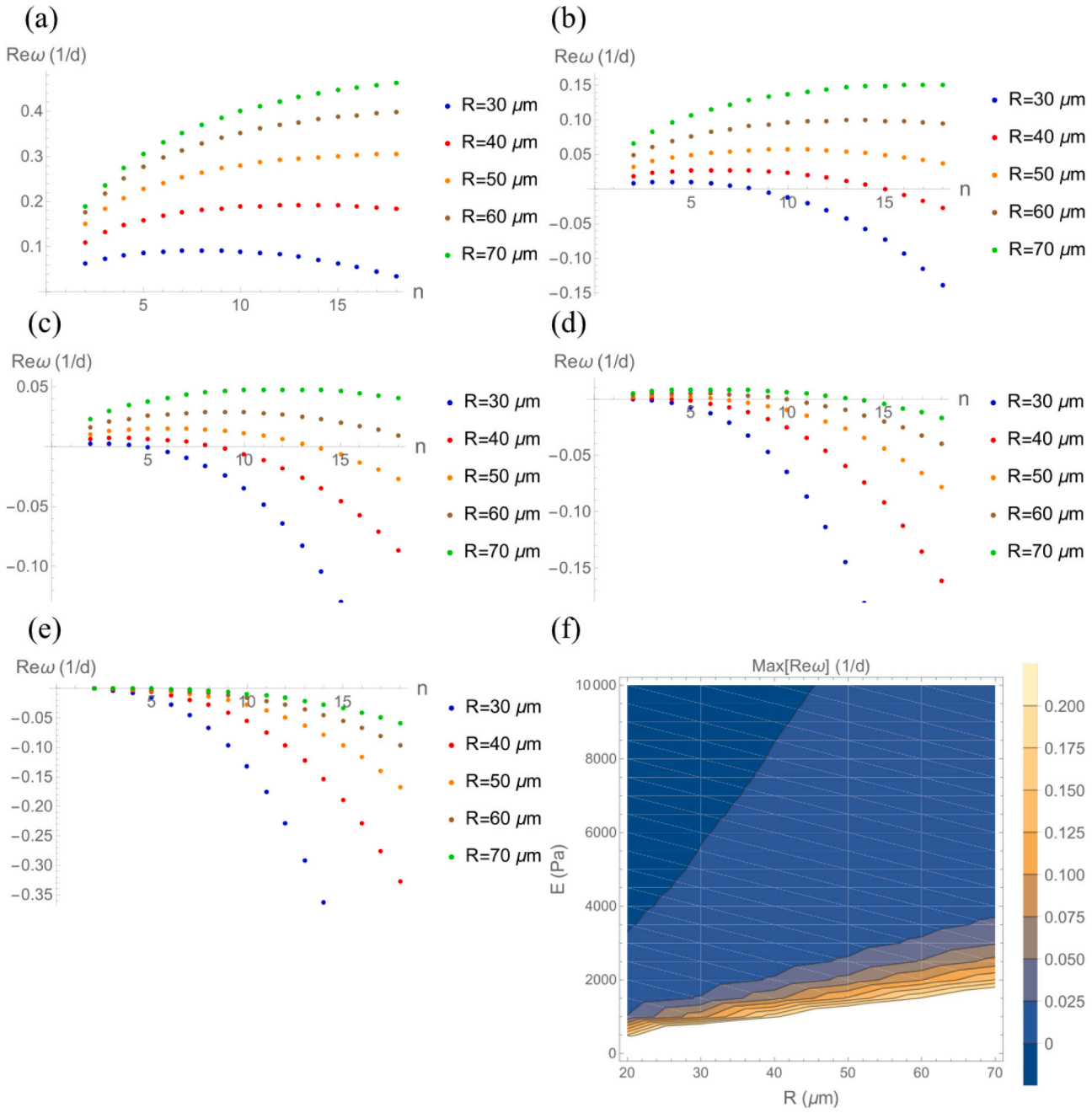

Fig. 5. (a-e) Relaxation modes ω as a function of the azimuthal wavenumber n for different radii of the tissue. (a) E=1*10^{3}Pa; (b) E=2*10^{3}Pa; (c) E=3*10^{3}Pa; (d) E=5*10^{3}Pa; (e) E=1*10^{4}Pa. (f) Maximal growth rate ω_{max} of a perturbation in different given E and R, demonstrated by the color scale. For all figures: ε=0.1, h=1 μm, other parameters are same as in Figs. 2, 3. (For interpretation of the references to color in this figure, the reader is referred to the web version of this article.)

and ω_{max} becomes close to 0. In the bottom right corner where the interface is most unstable, and ω_{max} is actually out of the color range, the maximum ω_{max} is approximately 1.0. The shortest characteristic timescale for perturbation to grow is then given by the $1/\omega_{max}=1d$. During steady state microstructure expansion, the stiffness of the BM and the radius of the tissue increase simultaneously while other parameters remain approximately constant. For the case we considered in the previous section, the expansion trajectory falls mostly into the blue region (the region occupies the largest area in the diagram) where ω_{max} is positive but close to 0. In this region, the characteristic timescale for perturbation amplification is in fact much longer than the timescale for tissue growth, so the interface largely maintains its unperturbed shape as the microstructure expands. After reaching its maximum size, the radius of tissue is fixed while BM continues to assemble. The parameters of the tissue will then transition into the dark blue region where ω_{max} is negative and any nascent fingers will decay with time.

4. Discussion

In this study, we provide theoretical interpretations of two distinct features observed during the non-linear expansion of human salivary stem cell derived microstructures. First, the observed coordinated tissue rotation is driven by the traction force at epithelium-BM interface. We show that rotation gradually decays as active propulsion force fails to overcome viscous friction and random noise. Next, the unexpected "popping" of the BM, in conjunction with the nontrivial cycling between rapid and slow expansion phases, originates from the different cell production rates under different compressive stresses. Compressive stress suppresses the division rate of cells as BM accumulates tensile strain. When reaching a strain threshold, the weak bonds in the BM break and the stretching tension immediately relaxes; this leads to a rapid expansion pulse, followed by a new round of BM organization and tension accumulation.

In the second part of our work, we analyzed system behavior under small perturbations of the interface. Here, we predict that a hydrodynamic instability may exist in our system. This instability is driven by the radial viscous shear stress due to the cell proliferation gradient. Increasing the maximum net cell production rate k and the viscosity of the tissue η can both destabilize the interface. Perturbations with smaller wavelengths are preferentially suppressed and the interface is more likely to evolve into wide fingers with long wavelength. The increasing radius of the microstructure is also a destabilizing factor as opposed to the Young's modulus of the BM. Since the stiffness of the BM and the size of the tissue increase simultaneously, this pair of opposite factors provides a guideline as to how to suppress undesirable interfacial instabilities during tissue growth. We note that in the experimental data of (Wu et al., 2019), no instability was seen. To test our theory and predictions, future experiments can artificially degrade the BM during different stages of microstructure expansion and genetically manipulate the cell cycle to decrease the thickness of proliferative cell layers.

In a recent study (Wang et al., 2021), Wang et al. performed live-organ imaging of mouse embryonic salivary glands at single-cell resolution. This study revealed that budding morphogenesis of stratified salivary gland epithelium is driven by the comparatively faster expansion and buckling of the surface epithelial sheet, constrained by the surrounding mesenchyme and the interior epithelium. There is a distinct difference in interfacial morphology between the salivary gland epithelium mentioned above and the tissue microstructure discussed in this paper. This difference may originate from the different cell types and culture systems, leading to different tissue growth modes and different mechanisms driving budding morphogenesis. In the paper of Wang et al., intact E13 mouse salivary gland, isolated single epithelial buds or dissociated single epithelial cells were used. Surface-originating cells would reinsert into the surface layer after dividing in the subsurface region. Therefore, compressive stress only accumulates in a single sheet conformally adherent to a non-expanding inner cell core. The in-plane stress can only be relieved by lateral deflection, resulting in buckling morphogenesis. In the paper of Wu et al. analyzed in this work (Wu et al., 2019), salivary stem/progenitor cells enriched from adult human salivary tissues were used. These cells are less differentiated and more proliferative than mature salivary epithelial cells. The tissue microstructure embedded in hydrogel expands outwards due to the global cell divisions. As a result, repeated cycles of cell division and cell-cell junction rearrangement can lead to the relaxation of static stresses and effective cell flows on long timescales, preventing in-plane elastic compression. Potential interface undulations can only be driven by the hydrodynamic instability related to proliferation differential in different directions. It remains unknown whether there might be a transition from hydrodynamic instability to buckling after the microstructure reaches the maximum size and progenitor cells are fully differentiated. Investigating this issue may necessitate longer-term imaging of the microstructure as well as cell lineage tracing.

In our approach, we have treated the epithelial microstructure as a 2D incompressible fluid; this is an obvious simplification for a flattened droplet morphology. The microstructure rotates in a clockwise or a counterclockwise fashion as determined by the direction of the active propulsion force. The assembly rate of the BM is taken to depend on the absolute tangential velocity at the tissue boundary. This is consistent with the experiments showing that both directions of rotation can be observed within the same gel (Wu et al., 2019). This theoretical framework is sufficient to interpret the non-linear dynamics during steady state expansion and capture the essence of possible hydrodynamic instabilities in these highly proliferative tissues. However, modifications can be made to generalize our model to three-dimensions and include rotations in two orthogonal directions. Although not detected by the brightfield live imaging of the microstructures in our case, anisotropic rotations can lead to anisotropic ECM organization and tissue elongation in drosophila egg chambers (L and David, 2011; Horne-Badovinac, 2014) as well as in human mammary gland organoids (Fernández et al., 2021). Besides, previous work reported that rotational movements could be partially restored after vanishing in large structures if the BM was digested by a collagenase/hyaluronidase treatment (Wang et al., 2013). This phenomenon may be induced by other mechano-transduction pathway and cannot be explained by current model. In addition, Wu et al. also reported a slight microstructure contraction before and after each significant rapid expansion pulse (Wu et al., 2019). This contractility is likely to be mediated by the actomyosin activity inside cells and may serve as a mechano-transduction pathway to promote local BM assembly or remodeling (Zhong et al., 1998; Harunaga et al., 2014). As expansion slows down due to cell division inhibition, the inward flow caused by this contraction may prevail at some time points and directions, leading to contractile fluctuations on the growth curve. The surface contraction may also contribute to stabilize the interface and hinder the amplification of protrusions. However, we cannot integrate this observation into our current incompressible-fluid-model, since the cell density is conserved and the microstructure can only expand outwards as new cells are added in. One possible approach is to extend our description of the tissue to a general viscoelastic fluid and couple the intracellular active contractile stress with the cell deformation for a given tissue size. We leave this extension as a future direction.

There are two nonlinear relationship assumptions in our model. The equation defining BM stiffness as a function of total BM components is chosen based on the fact that most BM proteins have multivalent binding sites and can build complex covalent as well as noncovalent cross-links (Chang and Chaudhuri, 2019; Khalilgharibi and Mao, 2021). The nonlinear equation describing the growth suppression in response to the BM compression was chosen based on the observation that microstructure expansion slows down rapidly after BM breaks and starts reorganization. Other works assume that growth rate decays exponentially under increasing compression (Montel et al., 2012). Although these nonlinear relationships may all capture the growth curve qualitatively,

accurate measurements of the connectivity of the BM network, the material properties of the BM, as well as the quantitative relationship between cell proliferation and stress would lead to a refinement of this model. Furthermore, the elastic compressive stress from the surrounding hydrogel are neglected in the stress continuity equation in this model. In our *in vitro* tissue culture condition, this simplification is likely to be valid because the BM is orders of magnitude stiffer than the surrounding hydrogel (Wu et al., 2019; Ghosh et al., 2005; Chaudhuri et al., 2020). However, the compression and constraint from stroma may play important role in multicellular aggregate proliferation in other cases such as tumor growth *in vivo* (Northcott et al., 2018). In those processes, the local mechanical environment outside BM cannot be neglected and the thinning/popping of BM may not appear. In addition, the compression from surrounding hydrogel will suppress the instability and globally decrease the growth rate of perturbations, leading to a more stable tissue interface. Besides this, other conclusions, including the physical mechanism of tissue interfacial hydrodynamic instability as well as the stabilizing/destabilizing factors, are still valid. Also, the traction force at epithelium-BM interface is assumed to be balanced with the shear stress exerted from the hydrogel, so the BM doesn't rotate with the tissue.

Finally, as already mentioned above, the rotation velocity during steady state expansion is not incorporated into the interfacial stability analysis. This reduction has no effect on the instability in phase 2 because coordinated rotational motion has vanished in this phase. However, whether the rotation in unperturbed state can alter the instability in phase 1 needs to be addressed in future work. Other interesting directions include how certain interfacial patterns are selected (Stoop et al., 2015), and whether the nonlinear superelastic properties of BM (Li et al., 2021) contributes to these processes. We leave these as future research problems.

CRediT authorship contribution statement

Two of the authors (Chen and Levine) designed the research, performed calculations and wrote the paper. The last author (Wu) helped analyze the data and helped compare predictions to experimental findings.

Data availability

Data will be made available on request.

Acknowledgments

We thank M. C. Farach-Carson, Danielle Wu and Shaohe Wang for valuable discussions. HL acknowledges the support of the NSF, grants nos. PHY-1935762 and PHY-2019745.

Appendix A. Supplementary data

Supplementary data to this article can be found online at https://doi.org/10.1016/j.cdev.2022.203803.

References

Alert, R., Blanch-Mercader, C., Casademunt, J., 2019. Active fingering instability in tissue spreading. Phys. Rev. Lett. 122, 88104.
Banerjee, S., Marchetti, M.C., 2019. Continuum models of collective cell migration. Adv. Exp. Med. Biol. 1146, 45–66.
Basan, M., Joanny, J.F., Prost, J., Risler, T., 2011. Undulation instability of epithelial tissues. Phys. Rev. Lett. 106, 1–4.
Bogdan, M.J., Savin, T., 2018. Fingering instabilities in tissue invasion: an active fluid model. R. Soc. Open Sci. 5.
Büscher, T., Diez, A.L., Gompper, G., Elgeti, J., 2020. Instability and fingering of interfaces in growing tissue. New J. Phys. 22.
Cerda, E., Mahadevan, L., 2003. Geometry and physics of wrinkling. Phys. Rev. Lett. 90, 4.
Chang, J., Chaudhuri, O., 2019. Beyond proteases: basement membrane mechanics and cancer invasion. J. Cell Biol. 218, 2456–2469.
Chaudhuri, O., Cooper-White, J., Janmey, P.A., Mooney, D.J., Shenoy, V.B., 2020. Effects of extracellular matrix viscoelasticity on cellular behaviour. Nature 584, 535–546.
David, G.-R., Karine, G., Stéphane, D., Françoise, B.-W., 2012. Soft matter models of developing tissues and tumors. Science (80-.) 338, 910–917.
Delarue, M., et al., 2013. Mechanical control of cell flow in multicellular spheroids. Phys. Rev. Lett. 110, 1–5.
Dolega, M.E., et al., 2021. Extra-cellular matrix in multicellular aggregates acts as a pressure sensor controlling cell proliferation and motility. elife 10, 1–33.
Fernández, P.A., et al., 2021. Surface-tension-induced budding drives alveologenesis in human mammary gland organoids. Nat. Phys. 17, 1130–1136.
Fiore, V.F., et al., 2020. Mechanics of a multilayer epithelium instruct tumour architecture and function. Nature 585, 433–439.
Ghosh, K., et al., 2005. Rheological characterization of in situ cross-linkable hysluronan hydrogels. Biomacromolecules 6, 2857–2865.
Gompper, G., et al., 2020. The 2020 motile active matter roadmap. J. Phys. Condens. Matter 32.
Han, Y.L., et al., 2019. Cell swelling, softening and invasion in a three-dimensional breast cancer model. Nat. Phys. 16.
Hannezo, E., Prost, J., Joanny, J.F., 2011. Instabilities of monolayered epithelia: shape and structure of villi and crypts. Phys. Rev. Lett. 107.
Hannezo, E., Prost, J., Joanny, J.F., 2012. Mechanical instabilities of biological tubes. Phys. Rev. Lett. 109.
Hannezo, E., Prost, J., Joanny, J.F., 2014. Theory of epithelial sheet morphology in three dimensions. Proc. Natl. Acad. Sci. U. S. A. 111, 27–32.
Harunaga, J.S., Doyle, A.D., Yamada, K.M., 2014. Local and global dynamics of the basement membrane during branching morphogenesis require protease activity and actomyosin contractility. Dev. Biol. 394, 197–205.
Horne-Badovinac, S., 2014. The drosophila egg chamber-a new spin on how tissues elongate. Integr. Comp. Biol. 54, 667–676.
Khalilgharibi, N., Mao, Y., 2021. To form and function: on the role of basement membrane mechanics in tissue development, homeostasis and disease. Open Biol. 11.
L, H.S., David, B., 2011. Global tissue revolutions in a morphogenetic movement controlling elongation. Science (80-.) 331, 1071–1074.
Laurent, J., et al., 2013. Multicellular tumor spheroid models to explore cell cycle checkpoints in 3D. BMC Cancer 13.
Lemke, S.B., Nelson, C.M., 2021. Dynamic changes in epithelial cell packing during tissue morphogenesis. Curr. Biol. 31, R1098–R1110.
Lenne, P.F., et al., 2021. Roadmap for the multiscale coupling of biochemical and mechanical signals during development. Phys. Biol. 18.
Li, J., Manikantan, H., 2021. Influence of interfacial rheology on viscous fingering. Phys. Rev. Fluids 6, 1–18.
Li, H., Zheng, Y., Han, Y.L., Cai, S., Guo, M., 2021. Nonlinear elasticity of biological basement membrane revealed by rapid inflation and deflation. Proc. Natl. Acad. Sci. U. S. A. 118, 1–6.
Liang, H., Mahadevana, L., 2011. Growth, geometry, and mechanics of a blooming lily. Proc. Natl. Acad. Sci. U. S. A. 108, 5516–5521.
Lin, S., Gu, L., 2015. Influence of crosslink density and stiffness on mechanical properties of type I collagen gel. Materials (Basel) 8, 551–560.
Marchetti, M.C., et al., 2013. Hydrodynamics of soft active matter. Rev. Mod. Phys. 85, 1143–1189.
Mark, S., et al., 2010. Physical model of the dynamic instability in an expanding cell culture. Biophys. J. 98, 361–370.
Montel, F., et al., 2012. Isotropic stress reduces cell proliferation in tumor spheroids. New J. Phys. 14.
Nelson, C.M., 2016. On buckling morphogenesis. J. Biomech. Eng. 138, 1–6.
Northcott, J.M., Dean, I.S., Mouw, J.K., Weaver, V.M., 2018. Feeling stress: the mechanics of cancer progression and aggression. Front. Cell Dev. Biol. 6, 1v12.
Notbohm, J., et al., 2016. Cellular contraction and polarization drive collective cellular motion. Biophys. J. 110, 2729–2738.
Pham, K., Frieboes, H.B., Cristini, V., Lowengrub, J., 2011. Predictions of tumour morphological stability and evaluation against experimental observations. J. R. Soc. Interface 8, 16–29.
Pozzi, A., Yurchenco, P.D., Iozzo, R.V., 2017. The nature and biology of basement membranes. Matrix Biol. 57–58, 1–11.
Ranft, J., et al., 2010. Fluidization of tissues by cell division and apoptosis. Proc. Natl. Acad. Sci. U. S. A. 107, 20863–20868.
Risler, T., Basan, M., 2013. Morphological instabilities of stratified epithelia: a mechanical instability in tumour formation. New J. Phys. 15.
Sekiguchi, R., Yamada, K.M., 2018. Basement membranes in development and disease. Curr. Top. Dev. Biol. 130. Elsevier Inc.
Stoop, N., Lagrange, R., Terwagne, D., Reis, P.M., Dunkel, J., 2015. Curvature-induced symmetry breaking determines elastic surface patterns. Nat. Mater. 14, 337–342.
Tanner, K., Mori, H., Mroue, R., Bruni-Cardoso, A., Bissell, M.J., 2012. Coherent angular motion in the establishment of multicellular architecture of glandular tissues. Proc. Natl. Acad. Sci. U. S. A. 109, 1973–1978.
Taubenberger, A.V., et al., 2019. 3D microenvironment stiffness regulates tumor spheroid growth and mechanics via p21 and ROCK. Adv. Biosyst. 3, 1–16.
Torras, N., García-Díaz, M., Fernández-Majada, V., Martínez, E., 2018. Mimicking epithelial tissues in three-dimensional cell culture models. Front. Bioeng. Biotechnol. 6, 1–7.
Trushko, A., et al., 2020. Buckling of an epithelium growing under spherical confinement. Dev. Cell 54, 655–668 e6.

Wang, H., Lacoche, S., Huang, L., Xue, B., Muthuswamy, S.K., 2013. Rotational motion during three-dimensional morphogenesis of mammary epithelial acini relates to laminin matrix assembly. Proc. Natl. Acad. Sci. U. S. A. 110, 163–168.
Wang, S., Matsumoto, K., Lish, S.R., Cartagena-Rivera, A.X., Yamada, K.M., 2021. Budding epithelial morphogenesis driven by cell-matrix versus cell-cell adhesion. Cell 184, 3702–3716 e30.
Williamson, J.J., Salbreux, G., 2018. Stability and roughness of interfaces in mechanically regulated tissues. Phys. Rev. Lett. 121, 238102.
Wu, D., Witt, R.L., Harrington, D.A., Farach-Carson, M.C., 2019. Dynamic assembly of human salivary stem/progenitor microstructures requires coordinated integrin-mediated motility. Front. Cell Dev. Biol. 7, 1–15.
Yang, Y., Levine, H., 2020. Leader-cell-driven epithelial sheet fingering. Phys. Biol. 17.
Yeh, W.T., Chen, H.Y., 2016. Hydrodynamics of stratified epithelium: steady state and linearized dynamics. Phys. Rev. E 93.
Zhao, M., et al., 2018. Rapid development of stable transgene CHO cell lines by CRISPR/Cas9-mediated site-specific integration into C12orf35. Appl. Microbiol. Biotechnol. 102, 6105–6117.
Zhong, C., et al., 1998. Rho-mediated contractility exposes a cryptic site in fibronectin and induces fibronectin matrix assembly. J. Cell Biol. 141, 539–551.